Estimation of azimuthally varying attenuation from surface seismic data

Ivan Vasconcelos* and Edward Jenner†

*Center for Wave Phenomena, Department of Geophysics, Colorado School of Mines, Golden, CO 80401, USA
†GX Technology - Axis Imaging Division, 225 East 16th Avenue, Suite 1200, Denver, CO 80203, USA

ABSTRACT

Observing the azimuthally varying seismic attenuation in data that show azimuthal velocity anisotropy could contribute not only to the interpretation of the subsurface symmetry systems, but also to the characterization of its physical parameters. In this paper, we estimate azimuthal variations of the P-wave effective quality factor (Q) from field surface seismic data. We also provide an interpretation of our results taking into account the NMO ellipse parameters measured from the data, and potential bias caused by systematic noise. By assuming that Q is frequency independent, and the medium at each particular azimuth the medium is laterally homogeneous, we use the spectral ratio method and a regularized linear inversion scheme to estimate the quality factor in azimuth-sectored data. The regularization parameters are chosen by a χ^2 criterion that is based on estimates of the variance in the field data. Tests on synthetic data show that this regularized inversion provides robust estimates of Q for signal-to-noise ratios lower than those observed in the data. Application of this methodology to P-wave data from the East Decatur Field in Texas yields non-negligible azimuthal variations in Q. The azimuthal signature of attenuation appears to be consistent with the effective NMO ellipse from the same interface. However, data residuals show non-random structures that suggest a strong systematic component to the noise. We provide a brief analysis of scattering-related absorption and of frequency imprints of source-receiver arrays as possible sources of systematic noise.

Key words: attenuation, azimuthal anisotropy, regularized inverse solution

1 INTRODUCTION

An important dynamic effect for wave propagation in elastic media is attenuation. In media containing aligned cracks on scales smaller than the dominant seismic wavelength there should be azimuthally variable signatures of attenuation. These azimuthal attenuation variations may be valuable tools in identifying and characterizing fractures in the subsurface. Fractured formations are also known for showing azimuthal velocity anisotropy signatures. Jenner (2001) used azimuthally varying normal-moveout (NMO) velocities and AVO signatures from P-waves to identify fracture zones at the Weyburn field in Canada. Adding shear-wave splitting analysis to the information obtained by Jenner (2001), Cardona (2002) was able to interpret the predominant anisotropic symmetry systems at the reservoir level at Weyburn. Cardona (2002) also suggested that shear-wave splitting at vertical incidence could be affected by changes in saturation for certain fracture rheologies.

It is somewhat intuitive to expect that formations that are anisotropic with respect to velocities should have associated signatures of attenuation anisotropy. Indeed, experiments conducted in anisotropic physical models (Hosten et al., 1987; Arts and Rasolofosaon, 1992) showed that not only attenuation has a directional dependence but also the magnitude of its anisotropy can be more significant than that of velocity. Another

experiment conducted by Prasad and Nur (2003) relates P-wave attenuation anisotropy to the texture of sedimentary rocks. Clark et al. (2001) estimated azimuthal variations of attenuation from four sail-line profiles extracted from a 3D marine dataset acquired offshore West Africa. Their interpretation of the principal orientation of the azimuthally variable attenuation is consistent with fracture orientations infered from azimuthally variable AVO.

Taking attenuation into account is also important because of its sensitivity to fluid content. Through 1D Biot equations for poroelastic media, Gurevich et al. (1997) provided an analytical description on how interlayer flow caused by wave displacement influences attenuation. From crosswell data collected at the Buena Vista Hills field, Hackert et al. (2001) used attenuation estimates in lithology identification which served as input to a later study by Parra et al. (2002), who used the information of higher attenuation zones to characterize fluid infill in fractured shale formations. Obtaining azimuthally variable estimates of attenuation can help not only in estimating the orientation of fractures, but also in characterizing some of their physical properties (Rathore et al., 1995; Lynn et al., 1999).

A common parameter used in attenuation estimation is the quality factor, or Q, which is inversely proportional to attenuation. There are many methodologies available for estimating Q. Dasgupta and Clark (1998) use the spectral ratio method to invert for Q using stacked power spectra extracted from stretch-compensated NMO-corrected gathers. In a physical modeling experiment Zhu (2005a) applies the spectral ratio method to analyze variations of attenuation with polar angle. Using prestack data, Hicks and Pratt (2001) apply a tomographic approach based on local descent methods to estimate the quality factor. Also in the context of surface seismic data, Zhang and Ulrych (2002) use the peak frequency shift in the power spectra from different time windows to invert for Q. Quan and Harris (1997) also rely on the peak frequency shift method in crosswell tomography to estimate attenuation. According to Mateeva (2003), Q can be estimated reliably from surface seismic as long as the subsurface can be described by a model with stationary reflectivity, bounded by a free surface. The methodology we describe in this paper makes use of the spectral ratio method (Mateeva, 2003; Dasgupta and Clark, 1998; White, 1992) to estimate Q.

Estimating Q related to intrinsic absorption may prove to be an involved procedure as scattering from thin layering also contributes to attenuation. In this paper, we use the term *effective Q* to refer to the total attenuation effect that is due to both intrinsic and scattering absorption. Mateeva (2003) describes a methodology to separate intrinsic absorption from multiple scattering effects in the context of check-shot VSP experiments. Her approach relies on well log reflectivity data to model only the scattering component of attenuation, which is then removed from the effective Q measurements. In Vasco et al. (1996) scattering absorption is predicted analytically by ray perturbation theory. We chose to model the scattering component of absorption in an approach similar to Mateeva (2003). With well log information, we can generate synthetic common-shot gathers using the reflectivity method (Müller, 1985) with only layering-induced absorption.

The main goal of this paper is to devise and implement a methodology that allows for azimuthally varying estimates of the quality factor. This project was inspired by the observation of azimuthal velocity anisotropy signatures in the East Decatur field that are likely caused by fracturing in the reservoir level. This observation suggested that there would be attenuation anisotropy signatures associated with velocity anisotropy. By assuming our model to be horizontally layered, laterally homogeneous and that Q only varies with azimuth we impose that any two trace pairs in a certain azimuth should yield the same estimate of Q. In practice we enforce the roughness penalty by means of Tikhonov regularization (Hansen, 1998). Since the reliability of our estimates is an important issue, error estimation is done by linear error propagation (Hansen, 1998; van Wijk et al., 2002). In order to obtain estimates of the variance in the data that are independent of model parameters, we use a nonparametric fitting approach (van Wijk et al., 2002; Grey and Silverman, 1994). We apply our methodology first to synthetic data and then to data from the East Decatur field. To describe one of the systematic noise components of the estimates from East Decatur we predicted the frequency response of scattering attenuation. Another source of systematic noise in our estimates are frequency distortions caused by stacking records from source and receiver arrays. Such noise is analyzed by computing the transfer functions of source and receiver arrays with the acquisition geometry of the East Decatur data. A simple formalism for computing array transfer functions is covered in Appendix B.

2 ESTIMATING THE QUALITY FACTOR

Since the objective of our study is to determine whether or nor it is possible to measure azimuthal variations of attenuation from the East Decatur field data, we need to design an inversion methodology that yields robust solutions in the presence of noise. Furthermore, it is of great importance for the chosen methodology to provide meaningful error estimates to determine if measured azimuthal variations of Q are representative of physical phenomena.

The vast majority of existing methods for Q inversion assume 2D media. The main reason for this is that until recently there were no models that presented a closed-form description of the azimuthal variation of Q.

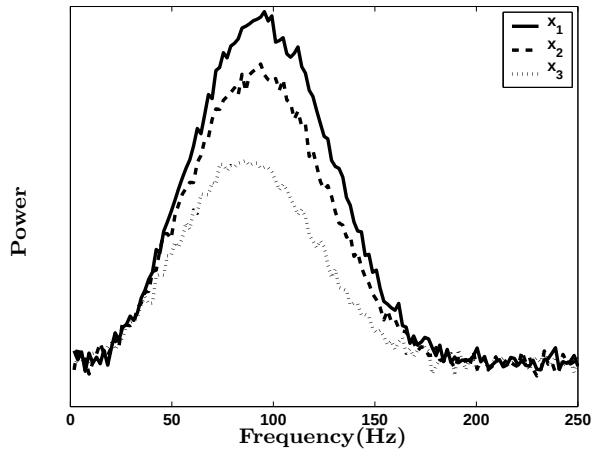

Figure 1. Noise-contaminated power spectra of the reflected signal for three traces with offsets $x_1 > x_2 > x_3$. Model parameters are the P-wave velocity $V = 2.0$ km/s, $Q = 250$ and the reflector depth 1 km. The source pulse was modeled with a Ricker wavelet. The bandwidth used in the inversion tests is $30 - 80Hz$.

In this paper, we assume that any vertical plane represents a section of horizontally layered, laterally homogeneous and isotropic medium. Such assumption allows us to use all data within a given narrow azimuth sector to obtain an estimate of the quality factor at that azimuth. It is therefore necessary to assume that the azimuthal variation of Q within a sector is negligible such that the medium can be considered as laterally homogeneous with respect to attenuation.

In a homogeneous isotropic attenuative medium, the spectrum of the signal at a certain trace j is given by:

$$S_j(f) = A_j\, W(f)\, e^{-\frac{\pi f t_j}{Q}} \tag{1}$$

where f is frequency, t_j is traveltime, Q is the quality factor of the medium and $W(f)$ is the spectrum of the source pulse. Here we will consider amplitude effects due to angle-varying reflectivity and geometrical spreading to be frequency independent, and these effects are accounted for by the term A_j in equation (1). From equation (1) we can see that attenuation in a homogeneous medium at a given frequency is a function of only the traveltimes, and Q . If we consider two signals recorded in the same medium and with the same source pulse, by dividing the spectra $S_1(f)$ and $S_2(f)$ of the waveforms recorded at traveltimes t_1 and t_2, we find:

$$\frac{S_1(f)}{S_2(f)} = \frac{A_1\, e^{-\frac{\pi f t_1}{Q}}}{A_2\, e^{-\frac{\pi f t_2}{Q}}} \tag{2}$$

Taking the logarithm of equation (2) gives;

$$\ln\left[\frac{S_1(f)}{S_2(f)}\right] = \ln\left[\frac{A_1}{A_2}\right] - \frac{\pi f}{Q}(t_1 - t_2) \tag{3}$$

Equation (3) shows that the quality factor Q can be directly estimated from the slope of the ratio of the spectra (in logarithmic scale) for any two traces, if the difference in traveltime between the traces is known. This is the so-called spectral ratio method for inverting for Q (Mateeva, 2003; Dasgupta and Clark, 1998; White, 1992). For later discussion, note that in equation (3) the absorption-related effects are contained in the slope term (frequency dependent), whereas all frequency-independent effects are contained in the intercept term.

According to equation (3), any two traces with a given azimuth can be used to obtain an estimate of Q. In an ideal case, this means that if we had an estimate for the quality factor for each possible trace pair for a gather with a fixed azimuthal orientation, then Q should always be the same. The methodology presented here seeks to take advantage of this "redundancy" by introducing a regularization operator. If there are N possible trace combinations in our azimuth gather, we can take the i^{th} trace pair and write our inverse problem based on equation (3) in the form of the following linear system:

$$\mathbf{A}_i\mathbf{m}_i = \mathbf{d}_i, \tag{4}$$

where,

$$\mathbf{A}_i = \begin{pmatrix} -\pi f_1 \Delta t_i & 1 \\ -\pi f_2 \Delta t_i & 1 \\ . & . \\ . & . \\ -\pi f_n \Delta t_i & 1 \end{pmatrix}, \tag{5}$$

$(f_1, f_2, ..., f_n)$ are the sampled frequency values corresponding to the spectral ratio values in $\mathbf{d}_i$ (left-hand side of equation (3)), and Δt_i is the traveltime difference between the two traces in the i^{th} trace pair. The matrix $\mathbf{m}_i$ contains the intercept and slope (proportional to $1/Q$) model parameters from the two terms in equation (3). Δt_i is computed from the hyperbolic two-way traveltime at each trace, taking into account the elliptical form of the azimuthal variation of normal-moveout velocity (Grechka and Tsvankin, 1998).

Our model objective function to be minimized in the inversion is designed in the following manner:

$$f(\mathbf{m}_i, \mathbf{s}) = \sum_{i=1}^{N} ||\mathbf{A}_i\mathbf{m}_i - \mathbf{d}_i||^2 + \lambda^2 ||\mathbf{R}\mathbf{s}||^2; \tag{6}$$

$\mathbf{s}$ is a $N \times 1$ matrix whose elements are the slope model parameters from all $\mathbf{m}_i$ ($1/Q$, Appendix A), $\mathbf{R}$ is a regularization matrix and λ is its regularization weighting parameter. This particular choice of $\mathbf{s}$ assures that we regularize our inverse problem only with respect to the slope term in equation (3), without imposing

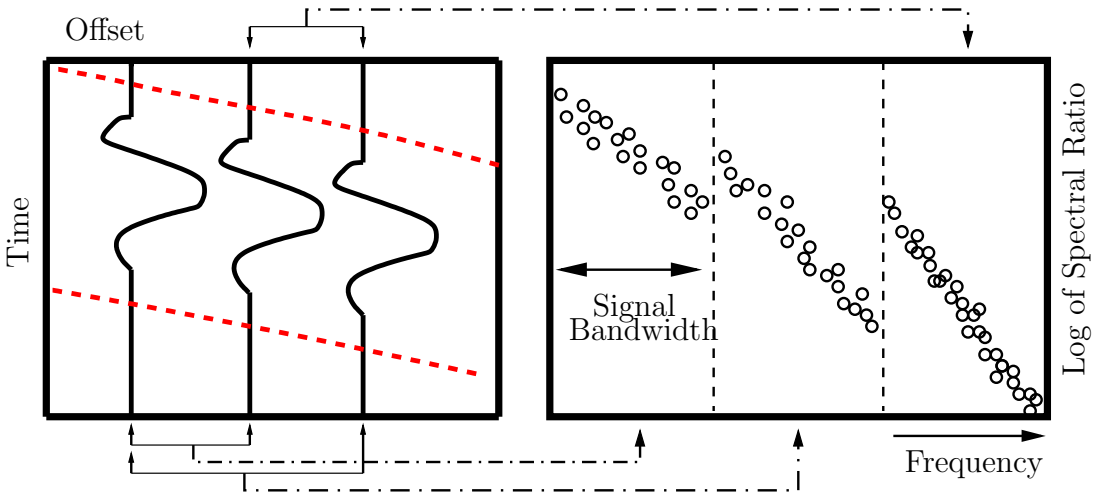

Figure 2. Generation of the data vector **d** (equation 8) from seismic traces using equation (6). Seismic data is sorted according to the CMP number and offset (left hand side). The waveform of the reflection event of interest is windowed on each trace (red dotted lines denote the time window). Then, for any two traces, we compute the ratio of the power spectra of the event (in logarithmic scale) on a sample-by-sample basis, which yields the data points on the right hand side panel in the figure. Each pair of traces provides the data $\mathbf{d}_i$, separated by the dashed lines.

any assumptions on the frequency-independent intercept term. The form of the objective function in equation (6) falls into the category of direct regularization methods known as Tikhonov regularization (Hansen, 1998).

The first term in equation (6) seeks to minimize the total misfit between the data (the spectral ratio) measured for each trace combination and data predicted by its corresponding $\mathbf{m}_i$. This term would be sufficient to carry out the inversion if the model assumptions were correct and the data were noise-free. Acknowledging the existence of non-negligible variance in our data, the second term in equation (6) penalizes the norm of $\mathbf{R}$ times the model. This allows us to find a solution that does not provide the minimum misfit, but complies to the model constraints enforced by $\mathbf{Rs}$. In our case, $\mathbf{R}$ is the sum of the first and second derivative operators. The regularized inverse operator related to the objective function in equation (6) can be found from its normal equations followed by simple linear operations that reduce our inverse problem to a single linear system. These steps are described in Appendix A. Our regularized inverse solution has the same form as the standard Tikhonov regularized inverse:

$$\mathbf{m}^{\dagger} = \mathbf{A}^{\dagger}\mathbf{d}, \tag{7}$$

where $A^{\dagger}$ is the so-called regularized pseudo-inverse operator,

$$\mathbf{A}^{\dagger} = (\mathbf{A}^T\mathbf{A} + \lambda^2\mathbf{R}^T\mathbf{R})^{-1}\mathbf{A}^T. \tag{8}$$

Substituting equation (8) into equation (7) gives

$$\mathbf{m}^{\dagger} = (\mathbf{A}^T\mathbf{A} + \lambda^2\mathbf{R}^T\mathbf{R})^{-1}\mathbf{A}^T\mathbf{d}. \tag{9}$$

The relationship between the matrices in equation (6) and in equation (9) are described in Appendix A. Of course, it would be simpler to just apply the Generalized Least Squares (GLS) solution (Hansen, 1998; Green and Silverman, 1994) and get independent estimates of attenuation for each trace pair. However, as we will see later on, if estimates of Q obtained independently for each pair, the actual inverted values for two noise-contaminated, closely neighboring trace pairs may be different by a factor of three. So, if we chose the best possible fit to the data (the GLS solution) we would violate the homogeneity assumption made in equation (3).

As mentioned earlier, it is important to provide meaningful model variances, such that the final results can be properly interpreted. The variance in the model parameters can be directly estimated from the inverse operator $\mathbf{A}^{\dagger}$ [equation (8)] and the data covariance matrix (Hansen,1998; van Wijk et al., 2002). For our particular case, we assume the data covariance matrix is a diagonal matrix of the data variances $\sigma_{d,i}$. To estimate the variance in the data ($\sigma_{d,i}$) we follow the approach described in van Wijk et al. (2002) and minimize the function

$$g(\mu_i) = ||\mu_i - \mathbf{d}_i||^2 + \lambda_{d,i}^2||\mathbf{R}_d\mu_i||^2 \tag{10}$$

with respect to μ_i, for a chosen operator $\mathbf{R}_d$. This gives us an estimate μ_{i,λ_d} for a given λ_d, a smoothed version of our data vector $\mathbf{d}_i$ according to the structure imposed by the operator $\mathbf{R}_d$. This type of fitting procedure is also know as nonparametric regression (Green and Silverman, 1994). If $\mathbf{R}_d$ is chosen so that it represents a certain structure present in the data, then the variance of $\mu_{i,\lambda_d} - d_i$ yields an estimate of $\sigma_{d,i}$ (van Wijk et al., 2002), the data variance with respect to the

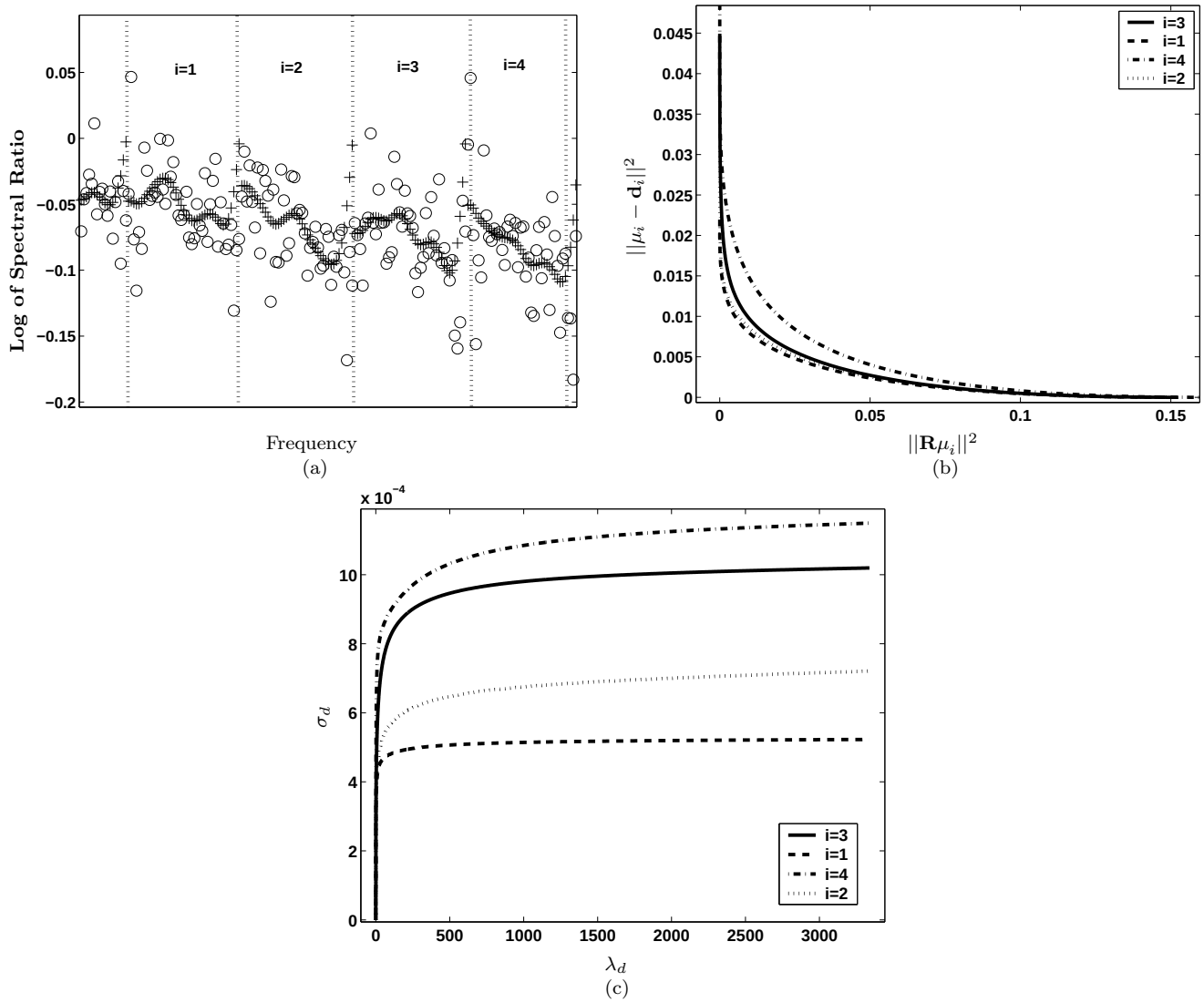

Figure 3. (a) Data from vectors $\mathbf{d}_i$ (equation 6) as in Figure 2(circles) and the smoothed data μ_i (equation 10, crosses). $\mathbf{d}_i$ were computed from noise-contaminated power spectra (Figure 1). The choice of $\lambda_{d,i}$ that gives μ_i can be done by picking $\lambda_{d,i}$ that yields the maximum curvature of L-curves in (b); for this value of $\lambda_{d,i}$ the data variance is approximately constant (c). Each of the four curves in (b,c) pertain to the data vectors $\mathbf{d}_i$ in (a). The data in (a) with $i = 1, 2, 3, 4$ have respectively increasing differences in offset.

structure predicted by $\mathbf{R}_d$. In our particular application we expect the data to have a linear dependence on frequency, hence we choose $\mathbf{R}_d$ to be a second derivative operator. The procedure of choosing the optimum λ_d will be described in the next section.

Another separate issue is determining the solution $\mathbf{m}^\dagger$. Once the regularized inverse operator is established, we can apply it to our data and obtain a regularized model. As in any other regularization problem, the choice of the weighting parameter λ determines $\mathbf{m}^\dagger$. For our particular application we apply a combined L-curve/χ^2 criterion. If the L-curve criterion (Hansen, 1998) alone is used, and the L-Curve varies smoothly, there is a wide range of λ values that satisfy the criterion but would result in vastly different models. If an estimate of the variance in the data is available, setting its corresponding χ^2 to some confidence level allows one

to compute a misfit cut-off for the L-curve that gives the best λ (van Wijk et al., 2002).

There are important practical issues related to the inversion methodology discussed above. To use equation 3 in our inversion scheme, we need to make an extra assumption. Since at a particular azimuth our model is supposed to consist of homogeneous layers with horizontal interfaces, while equation (3) is valid for homogeneous half-spaces, the contrasts between layers are assumed to be small and raypaths should be close to vertical. In practice, this assumption is enforced by only taking into account only near-offset traces (i.e., offset-to-depth ratio less than 1).

The forward operator $\mathbf{A}_i$ [equation (3)] and the data vector $\mathbf{d}_i$ pertain to a windowed portion of the corresponding traces containing the reflection event of interest. The center of window is equal to to the traveltime of the event predicted using the estimated moveout parameters for the corresponding CMP gather. Once the window center positions are determined, the windowing is carried out with a Hanning-type taper (Priestley, 1981). Mateeva (2003) discussed some of the implications of windowing in the Q estimation process. Her studies show that the window size imposes a bias on attenuation estimates, and this bias decreases with increasing window size. Our window size was typically on the order of 1.5 times the dominant wavelength of the signal. Mateeva (2003) also shows that windowing data with no tapering can severely distort estimates of Q, but the choice of the tapering function has little influence on the results.

After windowing, we pad the time series with zeros (for as many as ten times the length of the windowed series) to ensure a dense enough sampling of the power spectra. Next, we determine the signal frequency bandwidth by comparing the spectrum of our windowed time series with the spectra from far-offset traces for time windows positioned before the first arrival. The reason for this is that data before the first arrival should be representative of background noise.

3 SYNTHETIC DATA TESTING

Since one of our assumptions about the data is that each vertical plane can be treated as a horizontally layered, laterally homogeneous medium, the main focus of our synthetic data test is to assess the performance of our inversion methodology on CMP-sorted, surface seismic data that would represent an azimuth sector. Given that our main objective is to study the robustness of the regularized inverse operator in the presence of noise, the simplest model for our synthetic example is that of a homogeneous, isotropic, attenuative layer. For such a model, we can predict the the power spectrum of the signal at any trace simply by using equation (1), and having as input our medium parameters and the power spectrum of the source pulse. The synthetic data were then modeled with P-wave velocity $V = 2.0$km/s, $Q = 250$, a reflector depth of 1km and a Ricker source wavelet. The data was then contaminated with Gaussian random noise. Noise variances in the synthetic spectra were chosen to be at least two orders of magnitude larger than that of real data traces for times before the first arrival. Figure 1 shows noise-contaminated power spectra of the reflected signal from four traces. Figure 1 also illustrates that as the traveltime increases (with increasing offset), the frequency peak of the power spectrum shifts towards lower frequencies. This behavior should always be observed in data for media were the constant Q assumption is valid, and the attenuation coefficient is proportional to frequency.

Once the synthetic power spectra were generated, we computed the data vectors $\mathbf{d}_i$ [equation 6)] by taking the natural logarithm of the ratio between the spectra of all possible trace pairs (Figure 2). Before we can find the regularized inverse solution, it is necessary to estimate $\sigma_{d,i}$ (the variance in the data). After many iterations over the value of $\lambda_{d,i}$ we produce the L-curves in Figure 3b. The choice of $\lambda_{d,i}$ can be made by picking some point where the L-curve has the maximum curvature. Another option for the choice of $\lambda_{d,i}$ comes from the curves in Figure 3c that show that as $\lambda_{d,i}$ increases, the data variance increases rapidly at first and then becomes approximately constant. A natural choice for the regularization parameter would be the value $\lambda_{d,i}$ at which the increase data variance is negligible. After establishing the optimum value for the regularization parameter, we can predict the modified data vector μ (Figure 3a) and the total data variance. For the data with the highest offset difference between the two traces ($i = 4$) the corresponding σ_d is smallest (Figure 3). This happens because all power spectra had their samples randomly distorted with the same variance and the ratios that correspond to spectra with a higher attenuation difference will show smaller variance. If the noise in our data is limited to random fluctuations in the power spectra, traces with larger offset differences will give more stable estimates of Q. As to the issue of how reliable the estimates of the data variances ($\sigma_{d,i}$) are, we refer to the work of van Wijk et al. (2002).

With an estimate for the variance in the data, we set a threshold for the maximum tolerable misfit for a certain confidence level, according to the χ^2 test for goodness of fit (van Wijk et al., 2002). This threshold can then be used to decide the amount of regularization we can impose in our data. In practice, we wish to be conservative about the model smoothness in such a way we choose the value of λ (equation 9) that provides a misfit under the confidence level threshold. Figure 4 illustrates the L-curve for $\mathbf{R}$, with the corresponding misfit threshold set by the χ^2 criterion. For the chosen λ we can find the regularized inverse solution (Figure 5a,c). Figure 5a,c shows that the regularized inverse solution is closer to the true model than the standard general-

ized least squares (GLS) solution. We can also observe that there is some structure in the regularized inverse solutions. This structure is related to the ordering of the data vectors $\mathbf{d}_i$ within d, which in turn is related to how traces are sorted in the input data.

If the data variance estimation procedure provided perfect estimates and we decided to push the regularization to higher confidence levels, the structure of the regularized solution would be somewhat less smooth, depending on where the misfit threshold (determined from χ^2) intersects the L-curve. The regularized inverse solution in Figure 5c is less structured and closer to true model than in Figure 5a because its solution requires less regularization, since the data variance estimate is smaller. Figures 5b,d show the fit of the regularized and GLS solutions, for most trace pairs it is hard to visually distinguish the regularized from the non-regularized fit. This difference is small because the traveltime difference between traces is small, which translates into small differences in attenuation magnitudes. However, the differences between the regularized and non-regularized solutions for the same data are quite noticeable.

There may be cases when a structure in the solution induced by the use of differencing-type regularization operators is unwanted (e.g. if the structure is very steep). Another option for regularizing our problem is to penalize the norm of the residuals between each model parameter and the mean (exemplified in Appendix A). This particular choice of $\mathbf{R}$ will eliminate the structures caused by applying differencing type regularization operators. However, since the cause of structured solutions usually is the presence of extreme values, depending on the difference between the outlier values and the mean of the remaining solutions, the overall mean of the model parameter shifts towards the outliers.

4 EAST DECATUR FIELD DATA

Our field data study was conducted on prestack 3-D wide-azimuth P-wave data acquired over the East Decatur field, located in North Texas. The formation of interest is the Barnett formation, which is composed of thick fractured shale beds. The Barnett shale is one of the largest producing gas reservoirs in the United States, and it has been reported that its best production rates come from wells drilled in areas where natural fractures were present. Hence, the detection of natural fractures a crucial step toward identifying and characterizing areas of better production for reservoirs like the Barnett shale.

Figure 6 shows an Inline section from the the East Decatur field data after 3-D zero-offset migration. The subsurface geology at the East Decatur field is close to horizontally layered (as dips are in the order of 2°), with mild lateral velocity variations. Apart from the structural simplicity, this particular dataset was chosen for pronounced lateral variations of the P-wave azimuthal

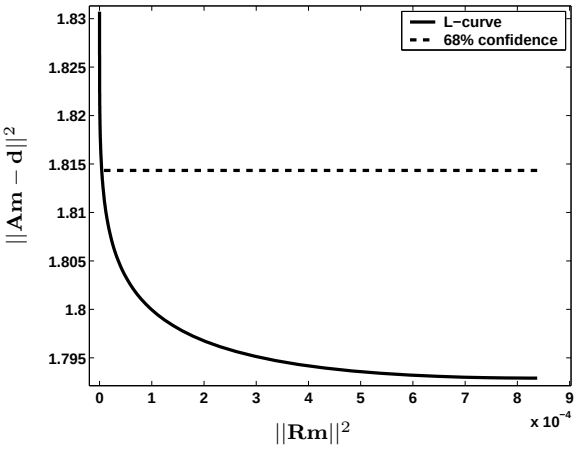

Figure 4. L-Curve for R [equation (8)]. Picking the value of λ corresponds to the misfit at the 68% confidence level results in the smoothest possible model according to the data variance.

anisotropy. Figure 7 shows NMO ellipse parameters for the reflection at the bottom of the Barnett formation. For this field, azimuthal anisotropy is mainly attributed to fractures in the Barnett shale beds since the interval NMO ellipse orientations coincide with fracture orientations from well observations and geologic data. The pronounced azimuthal velocity anisotropy signatures related to intrinsic properties (fracturing) of the Barnett formation immediately raised the question of whether there should associated azimuthal variations of attenuation anisotropy. The goal of the project was to obtain azimuthally variable estimates of the total effective attenuation and check if the results are in agreement with fracture orientations and velocity anisotropy signatures.

We applied the inversion methodology described above to estimate the azimuthally varying Q. The seismic data were sorted into CMP geometry, and the only pre-processing step applied was source-receiver statics. Because the windowing of the desired events is based on predicting reflected traveltimes, static corrections are important to assure proper windowing. Here, we show the azimuthal attenuation analysis for two 9×9 superbins, hereafter referred to as CMP1 (inline coordinate 1380, crossline 5285, Fig. 7) and CMP2 (inline 1398, crossline 5292), respectively. Traces were then sorted into 5° azimuth bins and the inversion for each bin was conducted for the horizon at approximately 1.3 s, interpreted as the reflection from the bottom of the Barnett formation. The window length was set constant to 98 samples, Figure 8a shows waveforms extracted from data traces. Their corresponding power spectra are displayed in Figure 8b. The real data spectra are smoother than the spectra in Figure 1 because random

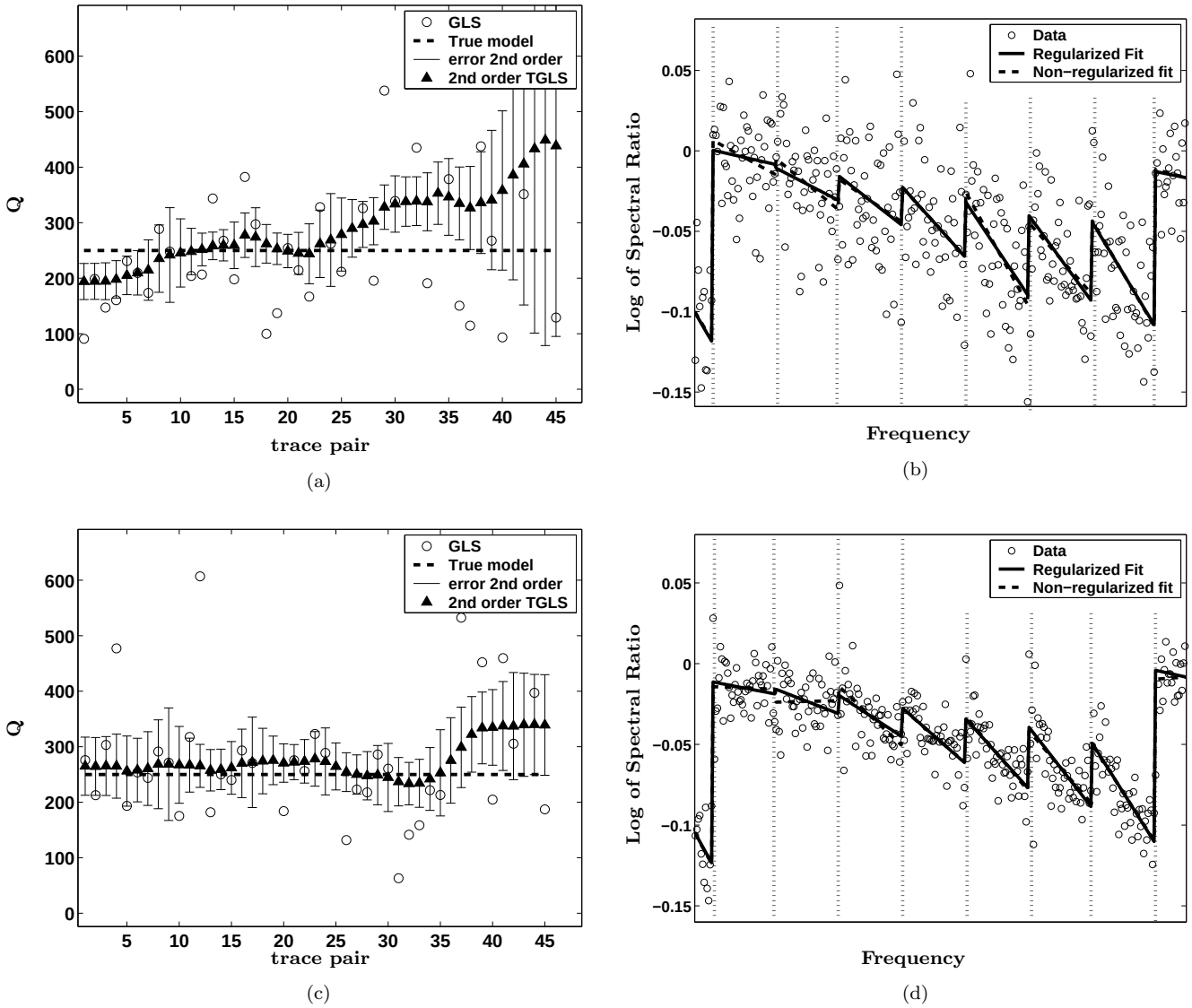

Figure 5. Inversion results for the synthetic data with different signal-to-noise ratios. The power spectra that generated data for (a,b) are distorted with twice the variance as the spectra for the results in (c,d). (a) and (b) show the Q estimates from the Tikhonov generalized least squares solution (TGLS, 2^{nd} order stands for the use of a first and second derivative operators in R, Appendix A) and the standard generalized least squares. The error bars represent the variance in the model parameters. (c) and (d) are the models fitted to the data, where the regularized fits are related to the TGLS solutions and the non-regularized fits pertain to the GLS solutions.

noise levels are likely smaller than those in synthetic tests.

Once the reflection event at a given azimuth bin has been windowed, we can set up our data space d [equation (8)] from the data vectors $\mathbf{d}_i$ computed for all trace pair combinations from offset-to-depth ratios up to 1.0. Next we estimate the variance in the data, which, from a simple visual examination of the smoothness of the power spectra (Figure 8) is expected to be less than the that in our synthetic examples. However, although there is little random noise in the spectra, we observe pronounced, repeatable, nonlinear structures in the spectral ratios (Figure 9b).

The algorithm described above treats these structures in the fit residuals as random noise. Clearly, the presence of non-random repeatable structures point to

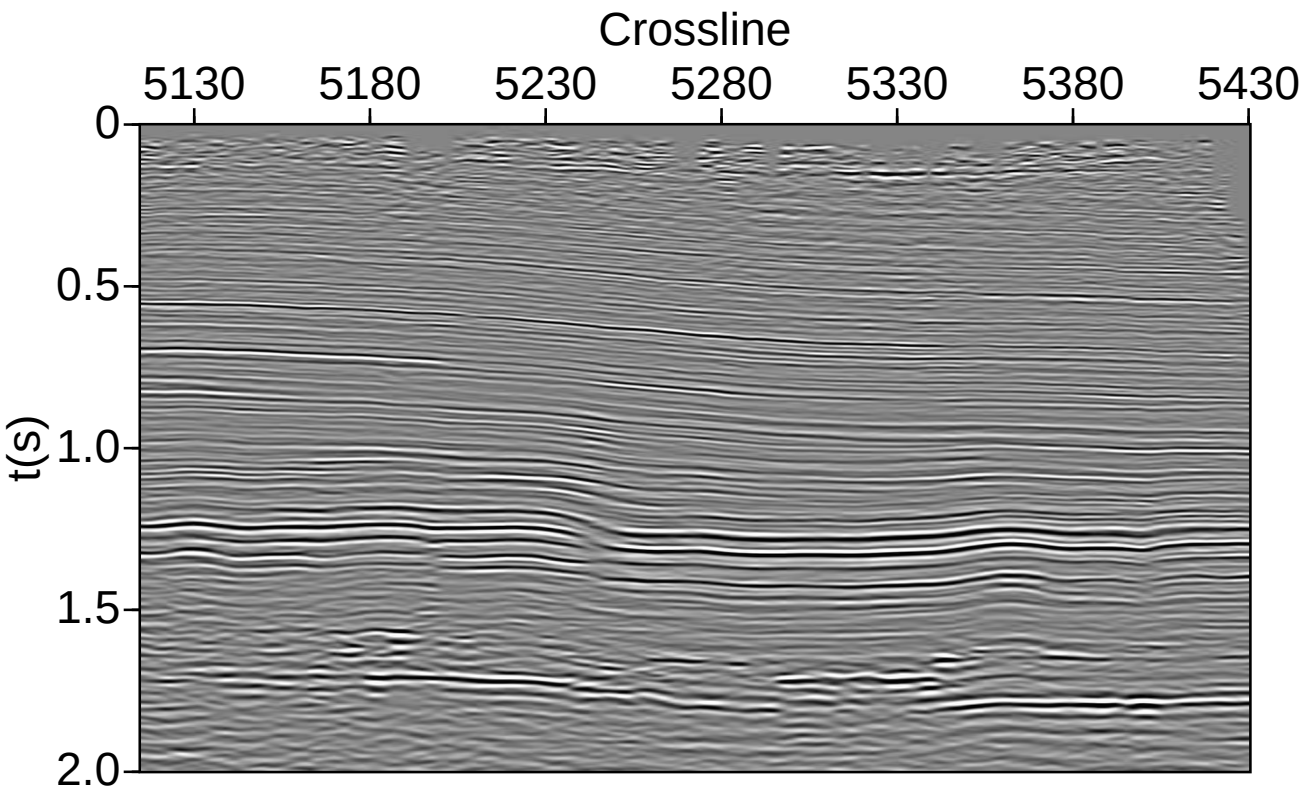

Figure 6. Post-stack migrated image of the East Decatur field data at Inline 1350. The Barnett shale formation is located approximately in the 1.0 s to 1.3 s interval. The overburden is composed of sand/shale sequences.

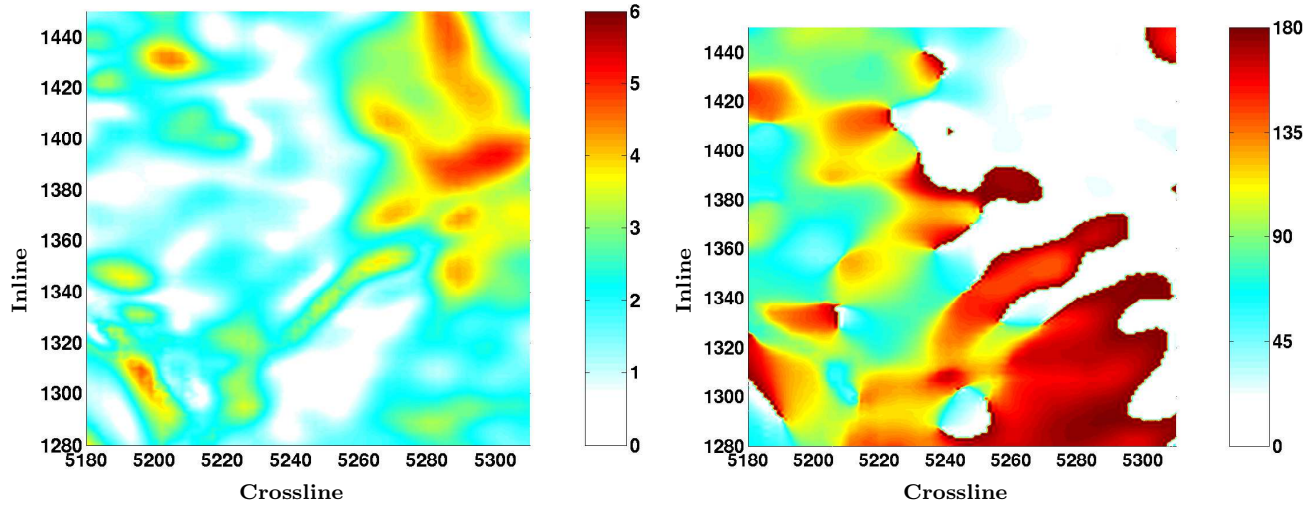

(a) (b)

Figure 7. Parameters of P-wave NMO ellipses for the reflection from the bottom of the Barnett formation in the East Decatur field. (a) The magnitude of azimuthal anisotropy (NMO ellipse eccentricities) in percent.(b) The orientation of the semi-major axis of the NMO ellipses with respect to North. The two CMPs analyzed (CMP1 and CMP2) lie within the area of stronger azimuthal anisotropy in the upper right-hand corner of the area, respectively with coordinates (*Inline* 1380, *Crossline* 5285) and (*Inline* 1392, *Crossline* 5292). Increasing Crossline coordinates point to the North.

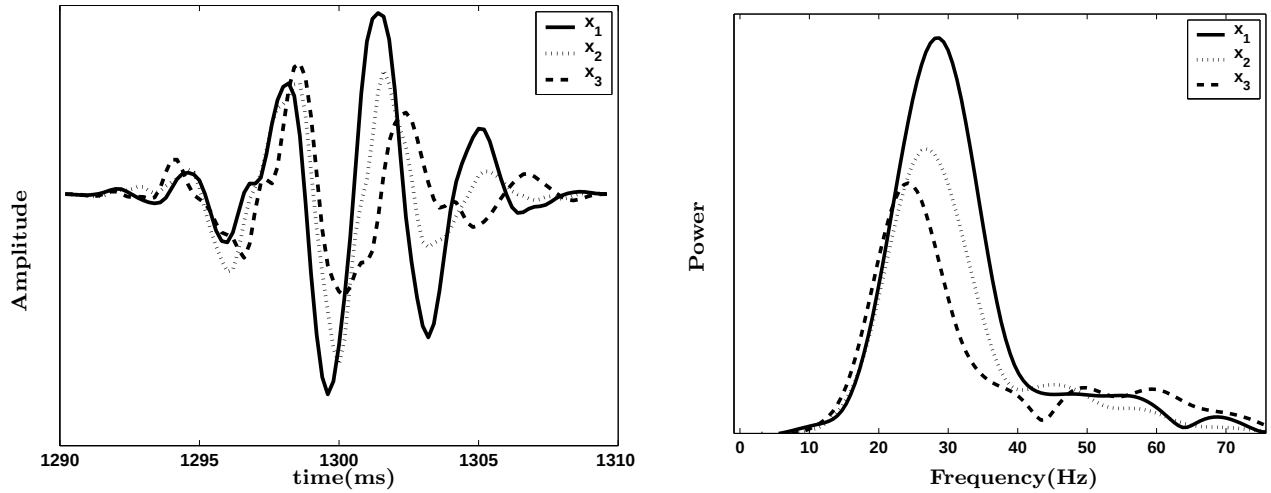

Figure 8. Widowed data from CMP1 for a 5° azimuth bin at an azimuth of 40° (a), and their corresponding power spectra (b). Offsets are $x_1 = 1614$ m, $x_2 = 1661$ m and $x_3 = 1708$ m. The inversion was carried out considering frequency samples from 25-50 Hz.

the fact that the assumptions do not account for all the relevant physical phenomena behind the data, although the model can represent a component of the data(Green and Silverman, 1994; Gu, 2002). In other words, we can take advantage of the fact that the regularization parameters can be tuned to set how much we impose a model structure. Then, it is possible to fit a linear component of the spectral ratio by trying to account for the fact that the data variances may be overestimated due to the presence of correlated noise components. We do this in practice by setting our λ to a value that corresponds to a misfit lower than the threshold set by the estimated σ_d. We can then try to pick a value of λ such that we get a model with reduced norm, at the same time being conservative towards the regularization as we try to keep the misfit and the regularization-induced bias as small as possible. Figure 9 shows the estimated model and corresponding data fit obtained following this approach, before and after regularization. To find the value of Q for a given azimuth, we chose to take the median of the regularized Q measurements for each trace pairs to minimize the contribution of outliers.

The effective quality factor for 5° azimuth bins with 20° azimuth increments are displayed for both superbins in Figure 10. It is clear from Figure 10 that if our assumptions and estimates of the variance in the data are accurate, there is a non-negligible azimuthal signature of attenuation. The direction of maximum attenuation (lowest Q) is close to the semi-minor axis of the NMO ellipse, approximately oriented East-West (Figure 7). If the fractures in the shale are fluid-filled, a possible physical interpretation is that waves traveling perpendicular to the most prominent set of fractures should have smaller velocities and experience higher attenuation. It is also interesting to observe that the magnitude of azimuthal attenuation anisotropy is much larger than that of azimuthal NMO velocity anisotropy. The interpretation of these results, however, has to include systematic components, which is discussed next.

If all or some of the nonlinear structure in the data is related to physical phenomena, it is not clear whether or not a linear fit to the data makes any physical sense. Here, we attempt to model nonlinear noise due to different physical phenomena, evaluate its influence on the data, and briefly discuss how it should be dealt with. Correcting for possible sources of noise and employing more involved parameter fitting techniques such as semiparametric fitting and residuals analysis (Grey and Silverman, 1998; Gu, 2002) would be preferable. These procedures, however, are beyond the scope of this paper.

We attribute the nonlinearities in the spectral ratios to two distinct physical phenomena. First, in our measurements we cannot separate the contribution of intrinsic absorption from that of layering-induced absorption. As it is discussed by Mateeva (2003), the attenuation caused by multiple scattering may influence the data in different ways, depending on the media properties. Second, for the East Decatur field, the data were

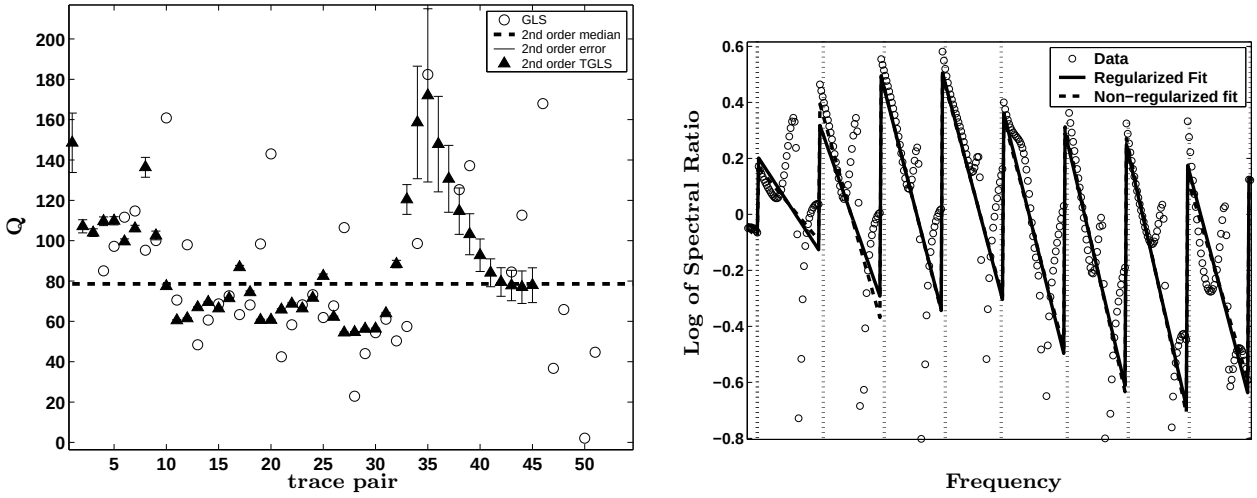

(a) (b)

Figure 9. Inverted parameter Q for a 5° azimuth bin from CMP1 at 40° azimuth (a), and the corresponding data fit (b). When compared to the synthetic results in Figure 5, Q measurements in (a) are more scattered, and the fit residuals in (b) exhibit non-random, repeatable structures.

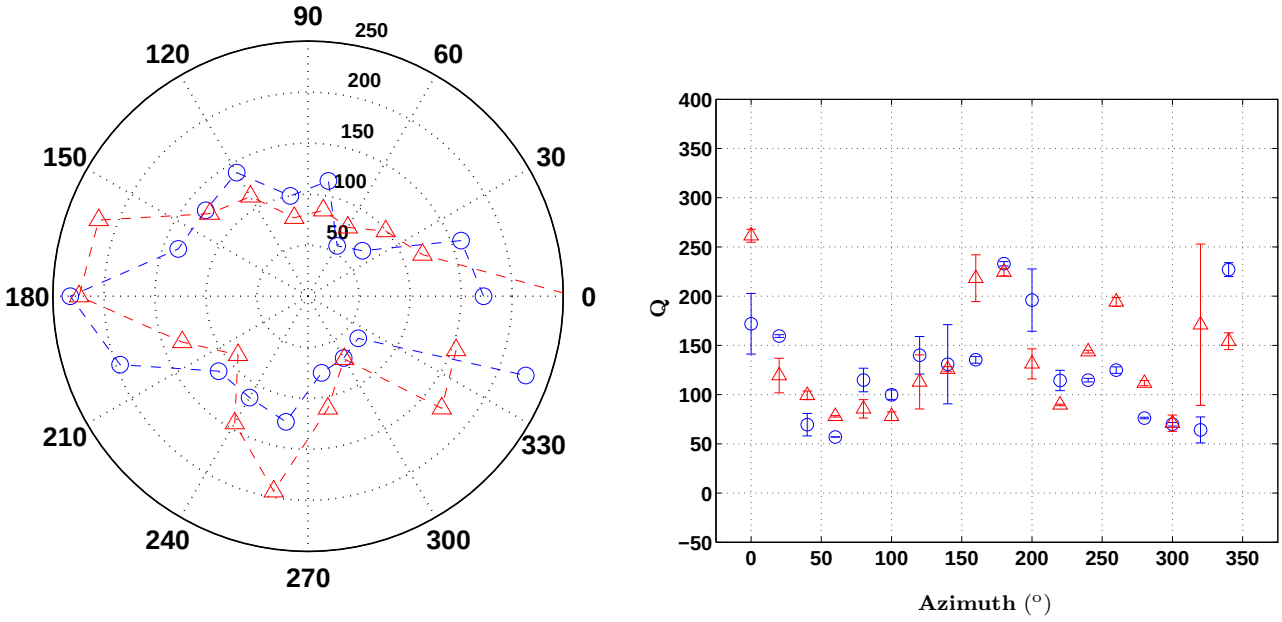

(a) (b)

Figure 10. Estimates of the effective quality factor at different azimuths shown in a polar plot (a) and with error estimates (b). The results from CMP1 are marked by the blue circles, and from from CMP2 by red triangles. The error bars in (b) are computed as the average standard deviation of the model variances for each trace pair within a sector (Figure 9). The azimuth is with respect to the North. The average orientation of the semi-major axis of the NMO ellipses is North-South.

acquired using source and receiver arrays. Since the response of each array component is simply stacked to form the data, the signature of the source-receiver arrays is frequency dependent (Appendix B).

For our particular dataset, it is also important to find out if multiple scattering due to thin layering could add a nonlinear component to the spectral ratios, and if this component has a structure that correlates to that observed in the data (Figure 9b). Using velocities (compressional and shear-wave) and densities from well logs, we generated a synthetic seismogram (Figure 11) for East Decatur with the reflectivity method (Muller, 1985). This method produces a complete wave-field with all multiples but no intrinsic absorption. Figure 12a shows that there is a clear offset-dependent nonlinear frequency imprint of scattering-induced attenuation in the spectral ratios. The data structure in Figure 12b is somewhat different from that observed in field data (e.g. Figure 9b), as field structures not only vary with offset, but also differ from one azimuth bin to another.

Even though layering-induced absorption causes nonlinear behavior in the spectral ratios, its influence should be azimuthally independent, as long as the medium is laterally homogeneous. This means that the bias in the estimates of Q related to multiple scattering should be the same at all azimuths. Also, in Figure 12 we can observe that the bias in the fitted slopes introduced by thin layering is offset dependent. This implies that if our data is not corrected for scattering absorption, the regularized solution may contain a structure related to the bias in each Q measurement, depending on how regularized the solution is. If too much smoothing (regularization) is applied to uncorrected data, it is difficult to assess how the bias from scattering absorption translates into errors in the estimated model parameters.

As discussed before, use of source and receiver arrays in acquisition creates frequency signatures that may distort the spectral ratios. In Appendix B we show how to obtain the frequency signatures of arrays for a simple homogeneous, isotropic model. For East Decatur field data, receiver arrays are composed of eight sensors, each at a distance of two meters from the center of the array with equal step in azimuth. Source arrays are made of a line of three vibrator trucks, with a 20 m separation between the trucks. The source line is always oriented in the direction 45°N. Because the spacing between the sources is considerably bigger than that between receivers in their respective arrays, the source array should produce a more substantial distortion in the power spectra. Also, there should be some azimuthal dependence of the source-receiver transfer function because the sources are set in a line with a fixed orientation for any source-receiver azimuth. The maximum contribution of the source array should be for the source-receiver azimuth that coincides with the source array orientation, and the minimum should correspond to the orthogonal direction (Appendix B). Using the results of Appendix B, we computed the frequency signatures of the source-receiver arrays for East Decatur data (Figure 13a,c). The biggest deviations of the spectral ratios occur at the 45^oN direction, while they become negligible at the 135^oN direction (Figure 13b,d). These azimuths coincide with the predicted directions of the maximum and minimum contribution of the source array, which confirms that the influence of the receiver array is relatively minor. Figure 13 also suggests that the bias in the spectral ratios induced by the source and receiver arrays varies with both offset and azimuth. Furthermore, the frequency dependence of this bias within the signal bandwidth can be considered as approximately linear. Hence, there will be an apparent azimuthal variation of attenuation due only to the particular geometry of the source and receiver arrays.

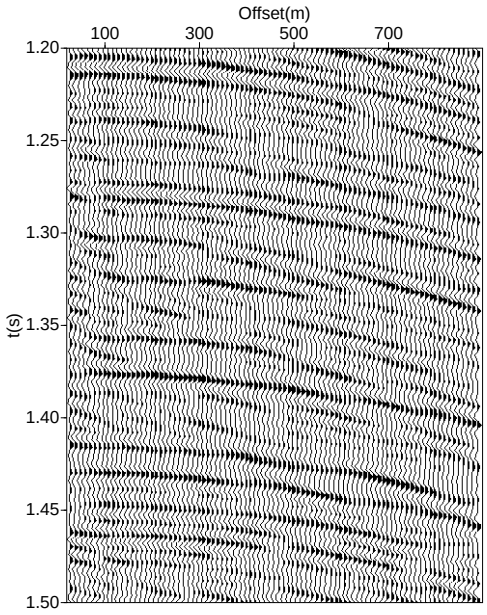

Figure 11. Synthetic seismogram of East Decatur data. The seismogram was computed using the reflectivity method with well log data as input. The event of interest in the seismogram is at approximately 1.28 s.

5 DISCUSSION AND CONCLUSION

With the objective of estimating the azimuthally varying attenuation, we proposed a methodology that assumes that at each azimuth the medium can be considered, as horizontally layered and laterally homogeneous. The methodology includes a search for a pseudo-inverse operator that can both fit the spectral ratio data and honor the model assumptions. In the regularization we

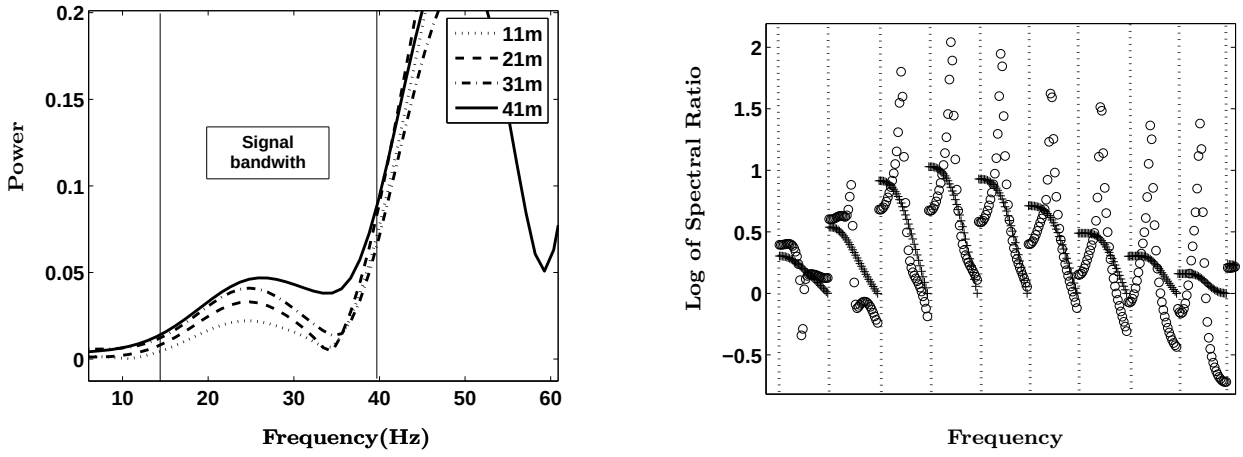

Figure 12. (a) Power spectra for the data modeled with the reflectivity method for the event of interest in Figure 11 at offsets 11, 21, 31 and 41 m. (b) Data vectors $\mathbf{d}_i$ (circles) and their smoothed versions μ_i (crosses), used to predict the variance in the data. The data in (b) are computed for the same bandwidth as the spectral ratios for the field data in Figure 9.

use equally weighted first and second derivatives operators to impose smoothness on the estimates of Q within each azimuth bin. This methodology is also designed to provide reliable error estimates. The variances in the model parameters are computed from the regularized pseudo-inverse operator and from the data variances obtained with a nonparametric fitting technique. The estimates for data variance also provide the basis for choosing the regularization weighting parameter.

Noisy synthetic data were generated by distorting power spectra with uncorrelated Gaussian noise. For this type of noise, estimates of Q from traces with larger traveltime differences tend to be more stable because the data variances are smaller. This synthetic test shows that even for signal-to-noise ratios smaller than those typically observed in real data, the regularized inverse solution is considerably closer to the true model than the standard generalized least squares (GLS) solution. While the regularized solution is always smoother than the GLS solution, for data with higher noise levels, it may contain structures that related to the particular order of the input data. In our case, this order is associated to the sorting of the field data traces.

In the East Decatur dataset, we applied our inversion methodology to two 9×9 CMP-sorted superbins that lie within one of the areas of strongest azimuthal velocity anisotropy. Since most of the azimuthal anisotropy observed in the East Decatur is is believed to be caused by the fracturing in the Barnett shale formation, our studies focused on the reflection from its bottom. The only pre-processing step applied to the data was source-receiver statics correction, which is necessary because the position of the window around the signal depends on reflected traveltimes computed from moveout parameters.

In contrast to the synthetic data, the spectral ratios from the field gathers contained very little random noise. Instead, we observed a strong nonlinear systematic component to the noise, which produces nonlinear structures in the spectral ratios. Because our methodology cannot separate systematic and random components of the noise, the data variance may be overestimated. In evaluating the linear component of the spectral ratios, we chose to avoid smoothing the data too much, keeping the misfit under the 68% confidence level threshold and the regularization-induced bias as small as possible. In this context, our results for the inversion for Q in 5^o azimuth sectors from both superbins show a similar azimuthally variable signature. The direction of the maximum attenuation is approximately East-West, which coincides with the average orientation of the semi-minor axis of the P-wave NMO ellipse.Taking fluid-filled fractures with a single predominant orientation as a model for the Barnett shale, maximum attenuation occurs in the direction perpendicular to the fracture strike. An important observation is that the magnitude of the azimuthal variations of attenuation is much larger than that of NMO velocities. In the context of East Decatur field, this suggests that attenuation measurements are much more sensitive to the anisotropy induced by the presence of fluid-filled cracks.

We considered two possible causes for systematic noise in the spectral ratios: absorption effects due to thin layering and frequency distortions caused by stacking the response of source and receiver arrays. We analyzed the first case by computing spectral ratio data for synthetic seismograms generated with the reflectivity

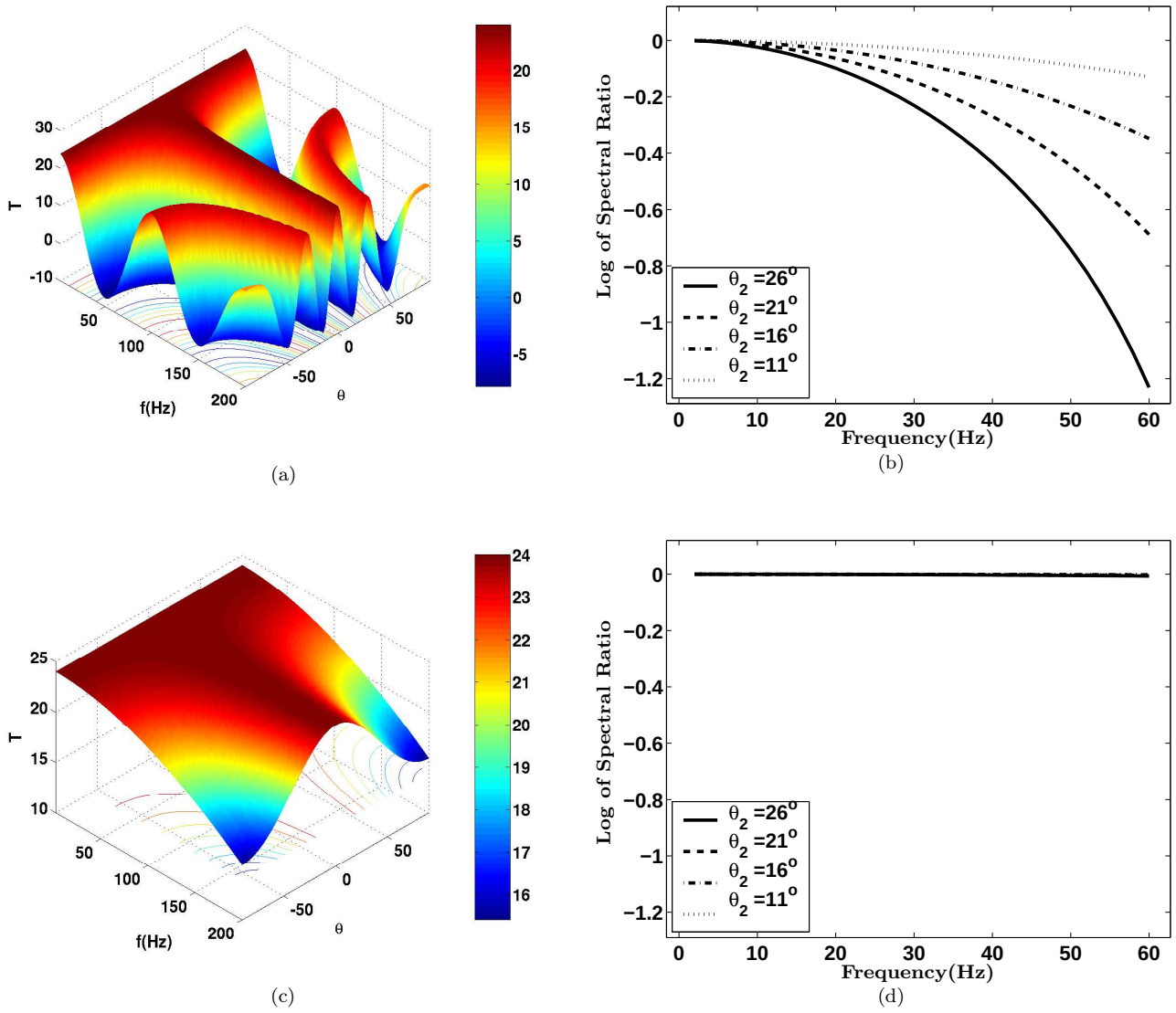

Figure 13. Transfer functions T, (a) and (c), of the source and receiver arrays combined as a function of the emergence angle θ and frequency ω. (a) Source-receiver transfer function for the source-receiver azimuth that yields the maximum frequency distortion (azimuth 45^{o}N), and (c), the source-receiver azimuth that gives the smallest frequency distortion. The frequency signatures in (a) and (c) translate into the signatures in the spectral ratios shown, respectively, in (b) and (d). Each curve on the spectral ratio plots is computed between one of the signals with the from the legend and a signal with the 5^o emergence angle. The same source and receiver array geometries used here were employed in the East Decatur field data acquisition. The emergence angles θ are directly related to offsets.

method. This way can generate shot gathers accounting only for the attenuation caused by multiple scattering for the reflectivity properties of the East Decatur field. Spectral ratios from the modeled data showed nonlinear features that change from one trace pair to the other, which suggests that the bias in slope estimation introduced by layering-induced absorption is a function of the trace offsets. For a horizontally layered, laterally homogeneous medium, attenuation effects due to multiple scattering are independent of azimuth.

To examine the frequency signatures of the source and receiver arrays, we computed their corresponding transfer functions using the source and receiver array geometries from field data. The frequency distortions in-

troduced by the receiver array are negligible compared to those caused the source array. Also, since the sources are set up in a line with fixed orientation, its frequency signatures are azimuthally dependent. These signatures translate into the spectral ratios with a weak nonlinear dependence on frequency. The source and receiver arrays introduce a negative bias in slope estimates from spectral ratios, which is a function of both offset and azimuth. This generates an apparent azimuthally variable attenuation effect due only to the source and receiver array geometry, where attenuation is strongest at the 45^oN direction and weakest at 135^oN.

By accounting for layering-induced absorption and for the array transfer functions we could not completely reproduce the structures in the spectral ratios from field data. Strictly, in attenuative media reflectivity and geometrical spreading should be frequency dependent because of velocity dispersion. These effects would be dependent on incidence angle, which in turn would yield structures in the spectral ratios that should vary with offset. Source and receiver radiation patterns in lossy media also become frequency dependent, and their effects in spectral ratios should be corrected for.

In azimuthally anisotropic attenuative medium, intrinsic absorption will have a dependence in polar angle as well as in azimuth (Zhu, 2005b). For the results presented in this paper we ignored the influence of the polar angle. However, the methodology presented here could be applied to trace clusters with different offset ranges to obtain an estimate of the dependence of attenuation with polar angle. With closed form expressions for anisotropic attenuation in terms of anisotropic parameters as in Zhu and Tsvankin (2004, 2005b), the methodology described here could be applied to characterize anisotropic attenuation. Furthermore, our inversion procedure can be applied to other types of datasets with redundant wave-field information (e.g. walkaway vertical seismic profiles, tomographic experiments), and to time lapse studies.

6 ACKNOWLEDGMENTS

We greatly appreciate the input given by Alex Calvert (GX Tech., AXIS) throughout the course of the project. We are thankful to Roel Snieder (CWP) for his help on the issue of array transfer functions. I.V. is grateful to Huub Douma, Ken Larner and CWP colleagues for insightful discussions. Our appreciation also goes to Ilya Tsvankin and Kasper van Wijk for reviewing this paper. We would like to thank GX Technology (AXIS Imag. Div.) and Devon Energy for giving permission to publish these results.

REFERENCES

Arts, R. J., and Rasolofosaon, P. N. J., 1992, Approximation of velocity and attenuation in general anisotropic rocks: 62^{nd} Ann. Intl. Mtg. Soc. Expl. Geophys., Expanded Abstracts, 640-643.

Cardona R., 2002, Fluid Substitution Theories and Multicomponent Seismic Characterization of Fractured Reservoirs: Ph.D. thesis, Colorado School of Mines.

Clark, R. A., Carter, A. J., Nevill, P. C., and Benson, P. M., 2001, Attenuation measurements from surface seismic - azimuthal variation and time lapse case studies: 63^{rd} EAGE Conference and Technical Exhibition, Expanded Abstracts, L-28.

Dasgupta, R., and Clark, R. A., 1998, Estimation of Q from surface seismic reflection data: Geophysics, **63**, 2120-2128.

Grechka, V., and Tsvankin, I., 1998, 3-D description of normal moveout in anisotropic inhomogeneous media. Geophysics **63**, 1079-1092.

Grey, P. J., and Silverman, and B. W., 1994, Nonparametric regression and generalized linear models: Monographs on Statistics and Applied Probability, **58**, Chapman & Hall.

Gu, C., 2002, Smoothing spline ANOVA models: Springer-Verlag New York, Inc.

Gurevich, B., Zyrianov, V. B., and Lopatnikov, S. L., 1997, Seismic attenuation in finely layered porous rocks: Effects of fluid flow and scattering: Geophysics, **62**, 319-324.

Hackert, C. L., Parra, J. O., Brown, R. L., and Collier, H. A., 2001, Characterization of dispersion, attenuation, and anisotropy at the Buena Vista Hills field, California: Geophysics, **66**, 90-96.

Hansen, P. C., 1998, Rank deficient and discrete ill-posed problems: numerical aspects of linear inversion: Society for Industrial and Applied Mathematics.

Hicks, G. J., and Pratt, R. G., 2001, Reflection waveform inversion using local descent methods: Estimating attenuation and velocity over a gas-sand deposit: Geophysics, **66**, 598-612.

Hosten, B., Deschamps, M., and Tittman, B. R., 1987, Inhomogeneous wave generation and propagation in lossy anisotropic rocks: application to the characterization of viscoelastic composite materials: J. Acoust. Soc. Am., **82**, 1763-1770.

Jenner, E., 2001, Azimuthal Anisotropy of 3-D Compressional Wave Seismic Data, Weyburn Field, Saskatchewan, Canada: Ph.D. thesis, Colorado School of Mines.

Lynn, H. B., Campagna, D., Simon K. M., and Beckham, W. E., 1999, Relationship of P-wave seismic attributes, azimuthal anisotropy, and commercial gas pay in 3-D P-wave multiazimuth data, Rulison Field, Piceance Basin, Colorado: Geophysics **64**, 1293-1311.

Mateeva, A., 2003, Thin horizontal layering as a stratigraphic filter in absorption estimation and seismic deconvolution: Ph.D. thesis, Colorado School of Mines.

Müller, 1985, The reflectivity method: a tutorial: Journal of Geophysics **58**, 153-174.

Parra, J. O., Hackert, C. L., and Xu, P., 2002, Characterization of low Q zones at the Buena Vista Reservoir, California: Geophysics, **67**, 1061-1070.

Prasad, M., and Nur, A., 2003, Velocity and attenuation anisotropy in reservoir rocks: 73^{rd} Ann. Intl. Mtg. Soc. Expl. Geophys., Expanded Abstracts, 1652-1655.

Quan, Y., and Harris, J. M., 1997, Seismic attenuation tomography using the frequency shift method: Geophysics, **62**, 895-905.

Rathore, J. S., Fjaer, E., Holt R. M., and Renlie, L., 1995, Acoustic anisotropy of a synthetic sandstone with a controlled crack geometry: Geophys. Prosp., **43**, 805-829.

Vasco, D. W., Peterson Jr., J. E., Majer, and E. L., 1996, A simultaneous inversion of seismic traveltimes and amplitudes for velocity and attenuation: Geophysics, **61**, 1738-1757.

van Wijk, K., Scales, J. A., Navidi, W., and Tenorio, L., 2002, On estimating errors in inverse calculations: Geophysical Journal Intl., **149**, 624-632.

White, R. E., 1992, The accuracy of estimating Q from seismic data: Geophysics, **57**, 1508-1511.

Zhang, C., and Ulrych, T. J., 2002, Estimation of quality factors from CMP records: Geophysics, **67**, 1542-1547.

Zhu, Y., and Tsvankin, I., 2004, Plane-wave propagation and radiation patterns in attenuative TI media: CWP Project Review, CWP-479, 125-142.

Zhu, Y., and Tsvankin, I., 2005a, Physical modeling and analysis of P-wave attenuation anisotropy in transversely isotropic media: CWP Project Review.

Zhu, Y., and Tsvankin, I., 2005b, Plane-wave attenuation anisotropy in orthorhombic media: CWP Project Review.

APPENDIX A: THE TIKHONOV GENERALIZED LEAST SQUARES SOLUTION

Since our objective is to impose smoothness in the measurements of Q from one trace pair to another, it is important to incorporate the linear systems from all trace pairs into a single linear system that sets up the so-called generalized least squares problem.

Our model objective function is:

$$f(\mathbf{m}_i, \mathbf{s}) = \sum_{i=1}^{N} ||\mathbf{A}_i\mathbf{m}_i - \mathbf{d}_i||^2 + \lambda^2||\mathbf{R}\mathbf{s}||^2 ; \quad \text{(A1)}$$

where the forward operators:

$$\mathbf{A}_i = \begin{pmatrix} -\pi f_1 \Delta t_i & 1 \\ -\pi f_2 \Delta t_i & 1 \\ . & . \\ . & . \\ -\pi f_n \Delta t_i & 1 \end{pmatrix} , \quad \text{(A2)}$$

for the i^th trace pair. There are n frequency samples in the signal bandwidth and Δt_i is traveltime difference between the two traces. The model parameters matrices $\mathbf{m}_i$:

$$\mathbf{m}_i = \begin{pmatrix} \frac{1}{Q_i} \\ a \end{pmatrix} , \quad \text{(A3)}$$

where Q_i is the Q measurement and a is the intercept of the line fitted to the spectral ratio. The data $\mathbf{d}_i$ contain the values of the natural logarithm of the spectral ratio that correspond to the frequency samples in $\mathbf{A}_i$. The vector $\mathbf{s}$ in equation (A1) contains all of the elements equal to the $1/Q_i$ elements from all of the $\mathbf{m}_i$ matrices, sich that:

$$\mathbf{s} = \begin{pmatrix} \frac{1}{Q_1} \\ \frac{1}{Q_2} \\ . \\ . \\ \frac{1}{Q_N} \end{pmatrix} . \quad \text{(A4)}$$

To find the solutions that minimize equation (A1), we must differentiate it with respect to all model vectors $(\mathbf{m}_1, \mathbf{m}_2, ..., \mathbf{m}_N, \mathbf{s})$, and set the result to zero:

$$\sum_{i=1}^{N} \frac{\partial}{\partial \mathbf{m}_i} ||\mathbf{A}_i\mathbf{m}_i - \mathbf{d}_i||^2 + \lambda^2 \frac{\partial}{\partial \mathbf{s}} ||\mathbf{R}\mathbf{s}||^2 = 0; \quad \text{(A5)}$$

From which we obtain the following normal equations:

$$\sum_{i=1}^{N} \mathbf{A}_i^T\mathbf{A}_i\mathbf{m}_i + \lambda^2\mathbf{R}^T\mathbf{R}\mathbf{s} = \sum_{i=1}^{N} \mathbf{A}_i^T\mathbf{d}_i ; \quad \text{(A6)}$$

Let $\mathbf{A}$ be a matrix that contains all of our $\mathbf{A}_i$'s [equation (A2)] such that:

$$\mathbf{A} = \alpha_{k,l}, \quad \text{(A7)}$$

here $\alpha_{k,l}$ are the elements of $\mathbf{A}$ with row k and column l. From here on we will use k and l to denote respectively row and column indices of any matrix. Its only nonzero elements are

$$\alpha_{x+n(i-1),2i-1} = -\pi f_x \Delta t_i, \; 1 < x < n \quad \text{(A8)}$$

and

$$\alpha_{x+n(i-1),2i} = 1, \; 1 < x < n \quad \text{(A9)}$$

where $1 < i < N$ and maps elements from $\mathbf{A}$ to the corresponding i^th trace combination. The index x scans over frequency samples. The matrix $\mathbf{A}$ has N times n (Nn) rows and $2N$ columns, and contains the information from the forward operators of all trace pair combinations. With $\mathbf{A}$ we can set up a linear system:

$$\mathbf{A} = \mathbf{m}\mathbf{d} \quad \text{(A10)}$$

where $\mathbf{m}$ contains all model matrices $\mathbf{m}_i$ and $\mathbf{d}$ contains all data matrices $\mathbf{d}_i$.

Now, to go from the normal equation in equation (A6) to the final form of the pseudo-inverse solution, let's rewrite the matrices $\mathbf{A}_i$, $\mathbf{m}_i$ and $\mathbf{d}_i$ in the following manner:

$$\mathbf{A}_i = \mathbf{\Gamma}_i\mathbf{A}, \quad \text{(A11)}$$

$$\mathbf{m}_i = \mathbf{\Omega}_i\mathbf{m}, \quad \text{(A12)}$$

$$\mathbf{d}_i = \mathbf{\Gamma}_i\mathbf{d}, \quad \text{(A13)}$$

where

$$\mathbf{\Gamma}_i = \gamma_{k,l}, \quad \text{(A14)}$$

$$\mathbf{\Omega}_i = \omega_{k,l}, \quad \text{(A15)}$$

with nonzero elements

$$\gamma_{x+n(i-1),x+n(i-1)} = 1;\ 1 < x < n\,,\ 1 < i < N \quad \text{(A16)}$$

$$\omega_{2i-1,2i} = 1;\ 1 < i < N \quad \text{(A17)}$$

both $\mathbf{\Gamma}_i$ and $\mathbf{\Omega}_i$ are square matrices of dimensions Nn and $2N$, respectively. Thus our new $\mathbf{A}_i$'s dimensions are $Nn \times 2N$, $\mathbf{m}_i$ is now $2N \times 1$ and $\mathbf{d}_i$ is $Nn \times 1$. Also, with the objective of designing the pseudo-inverse operator, we can simply replace $\mathbf{s}$ by $\mathbf{m}$, and make sure $\mathbf{R}$ only operates on the slope terms by setting his elements that correspond to intercept terms to zero. This way, we can use equation (A12) and equation (A13) to rewrite equation (A6):

$$(\sum_{i=1}^{N} \mathbf{A}_i^T \mathbf{A}_i \mathbf{\Omega}_i)\mathbf{m} + \lambda^2 \mathbf{R}^T \mathbf{R}\mathbf{m} = (\sum_{i=1}^{N} \mathbf{A}_i^T \mathbf{\Gamma}_i)\mathbf{d}\,; \quad \text{(A18)}$$

From equation (A11) and equation (A16), the sum of all $\mathbf{A}_i$ over N results in $\mathbf{A}$. Likewise, summing $\mathbf{\Omega}_i$ and $\mathbf{\Gamma}_i$ over N results in identity matrices. When then get:

$$\mathbf{A}^T\mathbf{A}\mathbf{m} + \lambda^2 \mathbf{R}^T\mathbf{R}\mathbf{m} = \mathbf{A}^T\mathbf{d}\,; \quad \text{(A19)}$$

From which we obtain the pseudo-inverse solution:

$$\mathbf{m}^\dagger = (\mathbf{A}^T\mathbf{A} + \lambda^2 \mathbf{R}^T\mathbf{R})^{-1}\mathbf{A}^T\mathbf{d}. \quad \text{(A20)}$$

To provide an example of the regularization operator $\mathbf{R}$, let us consider:

$$\mathbf{R} = \begin{pmatrix} 1-\frac{1}{N} & 0 & -\frac{1}{N} & 0 & ... & 0 & -\frac{1}{N} \\ -\frac{1}{N} & 0 & 1-\frac{1}{N} & 0 & ... & 0 & -\frac{1}{N} \\ . & . & . & . & . & . & . \\ . & . & . & . & . & . & . \\ -\frac{1}{N} & 0 & -\frac{1}{N} & 0 & ... & 0 & 1-\frac{1}{N} \end{pmatrix}. \quad \text{(A21)}$$

This would be the regularization operator to be used if we choose to penalize the norm of the residuals from the mean of the model parameters. All the zeros in equation (A21) correspond to the intercept terms in $\mathbf{m}$.

APPENDIX B: TRANSFER FUNCTIONS OF SOURCE AND RECEIVER ARRAYS

Let us consider an array geometry according to Figure A1. From such geometry, we can define the quantities $R = |\vec{r} - \vec{c}|$ and $d(\vec{p}) = |\vec{p} - \vec{c}|$. If we simply stack the responses of the array components, then the total displacement $\vec{u}$ of the array:

$$\vec{u}(\omega, \vec{r}) = S(\omega) \int_C G(\vec{r}, \vec{p}) d\vec{p} \quad \text{(B1)}$$

where $S(\omega)$ is the source function in the frequency domain, and $G(\vec{r}, \vec{p})$ is the Green's function of the medium between $\vec{r}$ and $\vec{p}$. C is a closed contour (away from the origin) over which array elements are placed.

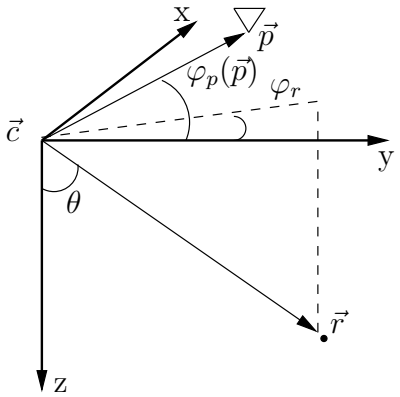

Figure A1. The array geometry used to derive the array's transfer function. An array centered at $\vec{c}$ has n array components with position denoted by $\vec{p}$. The array records an arrival from $\vec{r}$ that makes an emergence angle θ with the vertical. The array element at $\vec{p}$ makes an angle of φ_p with the x-axis, and $\vec{r}$ makes an angle of φ_r.

For a point force source in a homogeneous, isotropic medium:

$$G(\vec{r}, \vec{p}) = \frac{e^{ik|\vec{r} + d(\vec{p})\mathbf{x_i}(\vec{p})|}}{|\vec{r} + d(\vec{p})\mathbf{x_i}(\vec{p})|}, \quad \text{(B2)}$$

k being wavenumber, and $\mathbf{x_i}(\vec{p})$ is a unit vector with the same orientation as $\vec{p} - \vec{c}$. For convenience, in equation (B2) we set the array center $\vec{c}$ to the origin of the coordinate frame. Then putting equation (B2) in equation (B1) we get:

$$\vec{u}(\omega, \vec{r}) = S(\omega) \int_C \frac{e^{ik|\vec{r} + d(\vec{p})\mathbf{x_i}(\vec{p})|}}{|\vec{r} + d(\vec{p})\mathbf{x_i}(\vec{p})|} d\vec{p}; \quad \text{(B3)}$$

and, if we assume $R >> d(\vec{p})$:

$$\vec{u}(\omega, \vec{r}) = \frac{S(\omega)}{R} \int_C e^{ik|\vec{r} + d(\vec{p})\mathbf{x_i}(\vec{p})|} d\vec{p} \quad \text{(B4)}$$

Now, we can write

$$|\vec{r} + d(\vec{p})\mathbf{x_i}(\vec{p})|^2 = R^2 + 2d(\vec{p})[\vec{r}.\mathbf{x_i}] + d^2(\vec{p}), \quad \text{(B5)}$$

with

$$\vec{r}.\mathbf{x_i} = R\, sin\theta\, cos(\varphi_p(\vec{p}) - \varphi_r). \quad \text{(B6)}$$

Because $R >> d(\vec{p})$ we can drop the term quadratic on $d(\vec{p})$. Next, by taking the square root of equation (B5) and performing a Taylor expansion of the radical on the right-hand side we get:

$$|\vec{r} + d(\vec{p})\mathbf{x_i}(\vec{p})|^2 = R + d(\vec{p})\, sin\theta\, cos(\varphi_p(\vec{p}) - \varphi_r). \quad \text{(B7)}$$

Which, if replaced in equation (B4), gives:

$$\vec{u}(\omega, \vec{r}) = S(\omega) \frac{e^{ikR}}{R} \int_C e^{ikd(\vec{p})\, sin\theta\, cos(\varphi_p(\vec{p}) - \varphi_r)} d\vec{p} \quad \text{(B8)}$$

or

$$\vec{u}(\omega, \vec{r}) = S(\omega)\, G(\vec{r}, \vec{c})\, T(\omega). \quad \text{(B9)}$$

Equation (B8) represents the total displacement $\vec{u}$ in terms of the source function $S(\omega)$, the Green's function at the center of the array $G(\vec{r},\vec{c})$ and the transfer function of the array:

$$T(\omega) = \int_C e^{ikd(\vec{p})\, sin\theta\, cos(\varphi_p(\vec{p})-\varphi_r)} d\vec{p}, \qquad \text{(B10)}$$

or simply,

$$T(\omega) = 1 + \int_C e^{ikd(\vec{p})\, sin\theta\, cos(\varphi_p(\vec{p})-\varphi_r)} d\vec{p}, \qquad \text{(B11)}$$

for an array with a component in its center. From equation (B10) we can see that if $d(\vec{p})$ is constant and the array geometry is such that for an array component with a given azimuth φ_p there is another component with azimuth $\varphi_p + \pi$ (i.e. C is symmetric with respect to the coordinate axes in the surface plane), $T(\omega)$ is a purely real function. The consequence of this is that there are only amplitude distortions related to stacking the response of array components, while arrival phases suffer no distortions. This is the case for the geometries in the East Decatur field data.

To incorporate the effects of both the source transfer function $T_s(\omega)$ and the receiver's $T_r(\omega)$ into the source-receiver array function $T_sr(\omega)$ we simply take the product:

$$T(\omega) = T_s(\omega)\, T_r(\omega), \qquad \text{(B12)}$$

with, for example,

$$T_r(\omega) = \int_{C_r} e^{ikd_r\, sin\theta\, cos(\varphi_{p_r}(\vec{p_r})-\varphi_r)} d\vec{p_r}, \qquad \text{(B13)}$$

$$T_s(\omega) = 1 + \int_{C_s} e^{ikd_s\, sin\theta\, cos(\varphi_{p_s}(\vec{p_s})-\varphi_r-\pi)} d\vec{p_s}, \qquad \text{(B14)}$$

these being the transfer functions to be used for East Decatur field geometries. The distance $d(\vec{p})$ is constant for both source d_s and receiver d_r. Since $\vec{r}$ is between the source and receiver, we add $-\pi$ to the argument of the cosine in the exponential of either the source or receiver array transfer function, in this case, to $T_s(\omega)$.